Pyroxenes microstructure in comet 81P/Wild 2 terminal Stardust particles

Damien JACOB[1*], Julien STODOLNA[1], Hugues LEROUX[1], Falko LANGENHORST[2], and F. HOUDELLIER[3]

[1]Laboratoire de Structure et Propriétés de l'Etat Solide, Université des Sciences et Technologies de Lille and CNRS,
UMR 8008, F-59655 Villeneuve d'Ascq, France
[2]Bayerisches Geoinstitut, Universität Bayreuth, D-95440 Bayreuth, Germany
[3]CEMES/CNRS, 29 rue Jeanne Marvig, 31055 Toulouse, France
*Corresponding author. E-mail: damien.jacob@univ-lille1.fr

Abstract–We report the examination by transmission electron microscopy (TEM) of four Stardust terminal particles extracted from two neighboring tracks (32 an 69). The particles are made of well-preserved crystalline grains dominated by low-Ca pyroxene ranging from nearly pure enstatite to pigeonite. Some olivine grains are also found, in chemical equilibrium with the surrounding pyroxenes. Various microstructures are observed, as a function of the composition of the grains. They include (100)-twinned pigeonite, clino/ortho domains in enstatite and exsolution in a Ca-rich grain. The microstructures are mostly consistent with a formation by cooling from high-temperature phases, which could be associated to igneous processes. Some dislocations in glide configuration are also present, probably attesting for small intensity shocks. Possible effects of the rapid heating/cooling stage and thermal shock associated to the collect are discussed. It appears that most of the microstructural features reported here are plausibly pristine.

INTRODUCTION

The first examinations of captured dust particles from comet Wild 2 have been carried out in laboratories since the NASA Stardust capsule successfully returned the samples to Earth in January 2006 (Brownlee et al. 2006). Preliminary examination period revealed that the Wild 2 particles have been more or less severely thermally modified by the capture process due to hypervelocity impact at 6.1 km s^{-1} into silica aerogel capture media (Zolensky et al. 2006). The shape of tracks and the presence of individual components dispersed along the track indicates that Wild 2 dust have been alternatively loose aggregates (Hörz et al. 2006; Zolensky et al. 2006) or large mineral grains that have fragmented along the tracks (Burchell et al. 2008). In all cases, the larger components have penetrated more deeply into the aerogel and are found as terminal particles. These terminal particles are usually coarse-grained crystalline material (over 1 micrometer) and are found relatively well preserved from thermal capture modification. They include CAI-like particles (Simon et al. 2006) and chondrule-like objects (Nakamura et al. 2008), which suggests that some Wild 2 material is comparable to already known chondritic meteorites from the asteroid belt (Ishii et al. 2008). These observations support also the view of particle formation in the inner region of solar nebula followed by a large-scale radial mixing of matter in the protoplanetary disk before accretion in the comet.

Terminal particles are dominated by coarse-grained silicate grains (olivine and pyroxene) with a wide compositional variation (Zolensky et al. 2008a). In this context, fine-scale analysis of pyroxene-bearing particles is of peculiar interest to estimate formation conditions because pyroxenes are good indicators of thermal and deformational events. "Two pyroxene" thermometry is a useful tool for constraining the equilibration temperature of igneous and metamorphic rocks. This method is based on the distribution of Ca, Fe, and Mg between orthopyroxene and clinopyroxene over the 700–1500 °C range of temperatures (e.g., Ross and Huebner 1979; Lindsley 1983; Lindsley and Andersen 1983; Davidson and Lindsley 1985). Mg, Ca, and Fe cations ordering is also used as geospeedometer (e.g., Zema et al. 2003). Pyroxenes easily incorporate minor elements such as Na, Al, Ti, Cr, and Mn, and their partitioning in the crystallographic sites is a sign of the conditions of phase formation. This also applies to rare earth elements (REE), which frequently display zoning because of their slow diffusion rate (e.g., Papike et al. 2005; Papike 1996). Unlike olivine, pyroxene grains frequently record complex exsolution textures during cooling, and this can be used to decipher the igneous history (e.g., McCalister and Nord 1981;
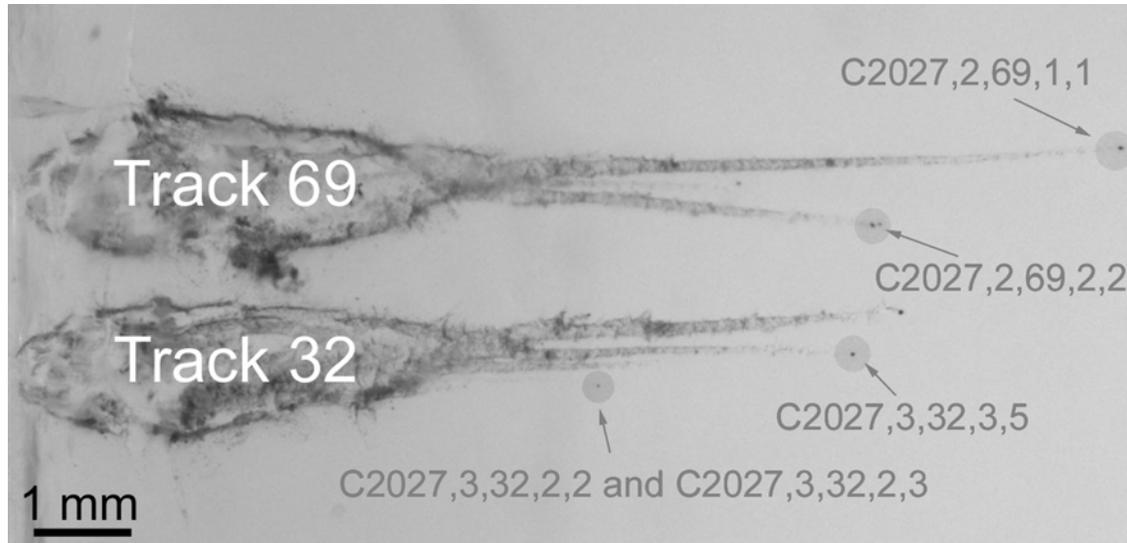
Fig. 1. Optical micrograph of tracks 32 and 69. (Image courtesy of NASA)

Leroux et al. 2004). Finally, pyroxenes are also known to display a wide variety of crystal defects, like, for instance, those occurring during shock deformation (e.g., Leroux et al. 1994; Langenhorst et al. 1995; Leroux 2001).

In this paper, we present data on the composition and microstructure of four pyroxene-rich terminal particles from Wild 2 studied by analytical transmission electron microscopy (ATEM).

SAMPLES AND ANALYTICAL PROCEDURE

The five Wild 2 samples analyzed in this study originate from four terminal particles of the neighboring tracks 32 and 69 from cell 27 (Fig. 1). They are TEM ultramicrotomed slices with the following labels: C2027,2,69,1,1: track 69, grain 1 (allocated to Univ. Lille), C2027,2,69,2,2: track 69, grain 2 (allocated to Univ. Lille), C2027,3,32,2,3: track 32, grain 2 (allocated to Univ. Lille), C2027,3,32,2,2: track 32, grain 2 (allocated to BGI Bayreuth), C2027,3,32,3,5: track 32, grain 3 (allocated to BGI Bayreuth).

The corresponding cometary grains were extracted from aerogel at NASA Johnson Space Center (JSC) Stardust curatorial facility. Details about extraction and manipulation can be found in Zolensky et al. (2008b). The extracted particles were embedded in EMBED-812 epoxy for serial sectioning using ultramicrotome equipped with a diamond knife. Each sample consisted of several TEM slices placed on a supporting carbon thin film stretched on a copper grid.

TEM results are acquired using a Phillips CM20 (Schottky field emitter operated at 200 kV, BGI, Bayreuth), a Philips CM30 (LaB$_6$ filament operated at 300 kV, Univ. Lille) and a FEI Tecnai G2-20 twin (LaB$_6$ filament operated at 200 kV, Univ. Lille). Chemical compositions are measured using energy dispersive X-ray spectroscopy (EDS) with Thermo-Noran and EDAX Si-detectors (CM30 and Tecnai,

respectively), and a Thermo-Noran Ge-detector (CM20). Analyses are recorded using a probe size ranging from 5 to 15 nm, either with a fixed probe for spot analyses or with a scanning probe for more spatially extended analyses and elemental distribution. Detailed description of analysis procedure and data reduction is given in Leroux et al. (2008a).

The microstructure of the samples is studied by conventional bright-field and dark-field imaging. For defect imaging, weak-beam conditions are used. High-resolution images are taken for fringe spacing measurements and planar defects characterization. Some high-resolution images have been obtained on the SACTEM-Toulouse (spherical aberration corrected TEM), a Tecnai F20 (FEI) equipped with a FEG source operated at 200 kV and an objective lens spherical aberration corrector (CEOS company). Among numerous advantages, the aberration correction enables the acquisition of good quality high-resolution images even for thick areas of the sample. Crystallographic data are obtained by selected-area electron diffraction (SAED). The CM30 (Univ. Lille) microscope is equipped with a Spinning Star precession module from the Nanomegas Company. Applying precession, the incident beam is scanned at a constant angle around the optic axis, in combination with a similar de-scan of the beam below the specimen (Vincent and Midgley 1994). The reflections are thus swept successively through the Ewald sphere and integrated intensities over a large range of deviation parameter are collected. Resulting diffraction patterns are thus always symmetric in intensity, even if the sample is not precisely oriented. Furthermore, dynamical interactions are strongly reduced, which limits the occurrence of double diffraction spots and makes the intensities more related to the structure factor. These points are of great use for the phase identification of small and imbricate crystallites as is the case in this study.
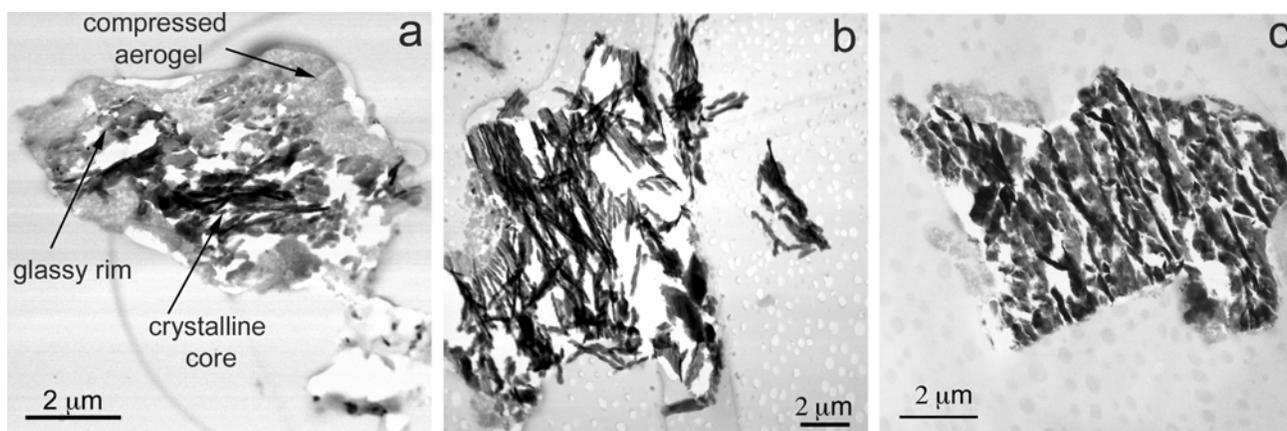
Fig. 2. Bright-field STEM images of samples a) C2027,2,69,1,1, b) C2027,2,69,2,2, and c) C2027,3,32,2,3. The sections are composed by a crystalline core surrounded by a dense silica-rich glass containing Fe-Ni-S phases and vesicles. Compressed aerogel is also present at the margin.

RESULTS

General Description and Compositions

The samples exhibit the same general aspect. They are made of a central area composed of crystalline shards partially overlapping due to the sample preparation. General views of the samples are shown in Fig. 2 for C2027,2,69,1,1, C2027,2,69,2,2, and C2027,3,32,2,3, showing various extent of damage relative to the preparation. A more or less broad rim of dense SiO_2-rich amorphous material surrounds the crystalline cores. Compressed aerogel is also frequently present at the margin. In sample C2027,2,69,1,1 (Fig. 2a), the glassy rim is much broader than in the other samples. This glassy material is silica-rich, with variable concentration of other elements. It contains Fe-Ni-S nanophases and large vesicles. Representative compositions are given in Table 1 for C2027,2,69,1,1. The characteristics of the glassy rim are quite comparable to those of the thermally modified particles which originate from melting and mixing of cometary material and aerogel (Leroux et al. 2008a).

The studied particles are dominated by low-Ca pyroxenes. C2027,2,69,1,1 is constituted of pigeonite with minor olivine, while the other samples are Mg-rich orthopyroxene, i.e., orthoenstatite. In C2027,2,69,1,1 and C2027,2,69,2,2 minor Ca-rich pyroxene is also found. Representative compositions are summarized in Table 2. In the following sections, we describe the microstructure of the two types of samples: pigeonite (C2027,2,69,1,1) and orthoenstatite (C2027,2,69,2,2, C2027,3,32,2,2/3 and C2027,3,32,3,5).

Pigeonite (C2027,2,69,1,1)

(100) Twinning

The dominant microstructure consists of a high density of lamellae parallel to the (100) planes (Figs. 3a, 3b). The (100) lamellae are roughly aligned from one shard to another, suggesting a common monocrystalline parent grain prior to the TEM preparation. Lamella widths range from 5 to 50 nm. These lamellae correspond to twinned domains as shown by the SAED pattern on Fig. 3c, which consists of the superposition of two monoclinic $P2_1/c$ phases, related by a mirror plane along (100). Distinction between the two monoclinic space groups of the pigeonite, namely the "high temperature" $C2/c$ and the "low temperature" $P2_1/c$, is made using the presence of h-odd $h00$ reflections. In the $C2/c$ space group, those reflections are kinematically forbidden ($h + k$ odd) and cannot appear by double diffraction, whereas they are visible in the $P2_1/c$ space group.

Inclusions: Olivine and Chromite

Small olivine grains, typically 200 nm in size, are also found as inclusions in the pigeonite host (Fig. 4a). Their composition ranges from Fo_{76} to Fo_{83} (Table 1). The Mg/(Mg + Fe) ratio close to that of the pigeonite host suggests a chemical equilibrium between the two phases. A second population of inclusions is occasionally present in the (100) habit planes of the pigeonite host (Fig. 4b). These inclusions are typically 20–30 nm in size, which is too small to be individually analyzed by EDS without including the pigeonite host. Nevertheless, spot analyses on the inclusions display strong Cr and Fe enrichments. Subtraction of the spectra from those recorded in the adjacent matrix strongly suggests that the inclusions are chromite ($FeCr_2O_4$). High-resolution images taken on the SACTEM-Toulouse clearly reveals the crystallographic orientation relationship of the {111} planes of the precipitates (spinel structure, space group Fd-$3m$) with the (100) planes of the pigeonite host (Fig. 4c). The Fourier transform diagram corresponds to a face-centered cubic structure oriented along a <110> zone axis. The {111} interplanar spacing is about 0.48 nm, which is compatible with the expected $FeCr_2O_4$ cell parameter (a = 0.830–0.838 nm).

Table 1. Representative EDS composition (at%) for sample C2027,2,69,1,1. The silica-rich glass compositions are from about 300×300 nm^2 wide areas. They are highly variables from place to place. For the pyroxene compositions, we have found a quasi-systematic SiO$_2$ excess, from 5 to 10 mol %. This excess probably originates from the adjacent silica glass that embedded the grains during the collect. In order to best report the cation distribution in the pyroxene structure, we subtracted this SiO$_2$ excess according to the ideal pyroxene structural formulae (M,Al)$_2$(Si,Al)$_2$O$_6$, with M are divalent cations and Al being for reason of charge compensation distributed between the tetrahedral and octahedral sites. For data reduction we used the following formulae: (Si + ½ Al) = (sum of the other cation + ½ Al). Once the excess of SiO$_2$ subtracted, the compositions were then renormalized to 100%. The same problem occurred for the olivine compositions. Since the tetrahedral sites in olivine is occupying only by Si, with a general structural formulae M$_2$SiO$_4$, we used the equation 2M = Si.

O	Si	Mg	Fe	Ni	S	Al	Ca	Cr	Mn
Silica-rich glassy areas									
62.3	27.1	6.0	1.4	0.1	1.5	0.8	0.3	0.1	0.3
63.3	28.4	4.5	1.8	0.1	1.0	0.5	0.3	0.1	0.1
62.2	26.9	5.4	2.8	0.1	1.3	0.5	0.4	0.2	0.1
Pigeonite									
60.1	19.6	13.8	4.2	nd	nd	0.9	0.7	0.6	0.2
60.0	19.7	14.2	4.0	nd	nd	0.7	0.9	0.3	0.2
60.1	19.6	14.2	4.2	nd	nd	0.8	0.8	0.1	0.2
60.2	19.5	14.4	3.6	nd	nd	1.0	0.4	0.6	0.2
60.2	19.6	13.8	3.9	nd	nd	0.8	0.8	0.6	0.3
High-Ca pyroxene									
60.1	19.4	8.6	3.0	nd	nd	1.2	7.2	0.3	0.3
Olivine									
55.7	13.9	23.0	7.0	nd	0.1	nd	nd	0.1	0.2
50.8	12.7	28.9	6.1	nd	0.2		nd	nd	0.4
57.2	14.3	22.6	5.6	nd	nd	0.1	0.0	0.0	0.1
57.2	14.3	23.3	3.7	nd	0.0	0.4	0.0	0.0	0.3

Table 2. Summary of the representative compositions (at%) for the four studied grains.

C2027,2,69,1,1	Pigeonite (Pi) $P2_1/c$ with minor olivine (Ol) and diopside (Di)	Pi: En$_{72-78}$Wo$_{2-6}$Fs$_{17-24}$ Ol: Fo$_{76-83}$Di: En$_{45}$Wo$_{39}$Fs$_{16}$
C2027,2,69,2,2	Orthopyroxene (Opx) with minor diopside	Opx: En$_{94-97}$Wo$_{1-4}$Fs$_{1-5}$Di: En$_{76}$Wo$_{21}$Fs$_3$
C2027,3,32,2,3	Orthopyroxene	En$_{91-95}$Wo$_{2-4}$Fs$_{3-6}$
C2027,3,32,3,5	Orthopyroxene	En$_{94-95}$Wo$_{2-3}$Fs$_{2-4}$

Dislocations

Dislocations lying in the (100) planes are found in pigeonite (Fig. 5a). They are visible with the diffraction vector $g = 002$ and are out of contrast with $g = 310$, which suggests a Burgers vector c and a screw character. Dislocations are also present in olivine (Fig. 5b). Observations with several diffraction vectors are compatible with dislocations having a Burgers vector c.

Damaged Areas

Locally, the pyroxene grains exhibit lamellar microstructures that appear damaged compared with those of the surrounding shards (Fig. 6a). The lamellar laths are roughly parallel to (100) planes, but are misoriented by a few degrees with respect to one another. Nevertheless, diffraction patterns of these areas indicate a common mean orientation with the surrounding undamaged twinned grains (Fig. 6b).

Composition analysis of these areas does not reveal any differences from the surrounding pyroxene grains.

Note that such damaged areas are not found in this sample only but are present in all observed samples. There occurrence may be due to the sample preparation by ultramicrotomy.

Enstatite (C2027,2,69,2,2, C2027,3,32,2,2/3 and C2027,3,32,3,5)

The four other samples are constituted of enstatite. A bright-field image of an enstatite grain in C2027,2,69,2,2 with the SAED pattern corresponding to the classical orthorhombic *Pbca* space group is reproduced on Fig. 7. In all the samples, the microstructure is characterized by the presence of (100) planar defects. Lattice fringe images (Fig. 8) reveal that they consist in the insertion of
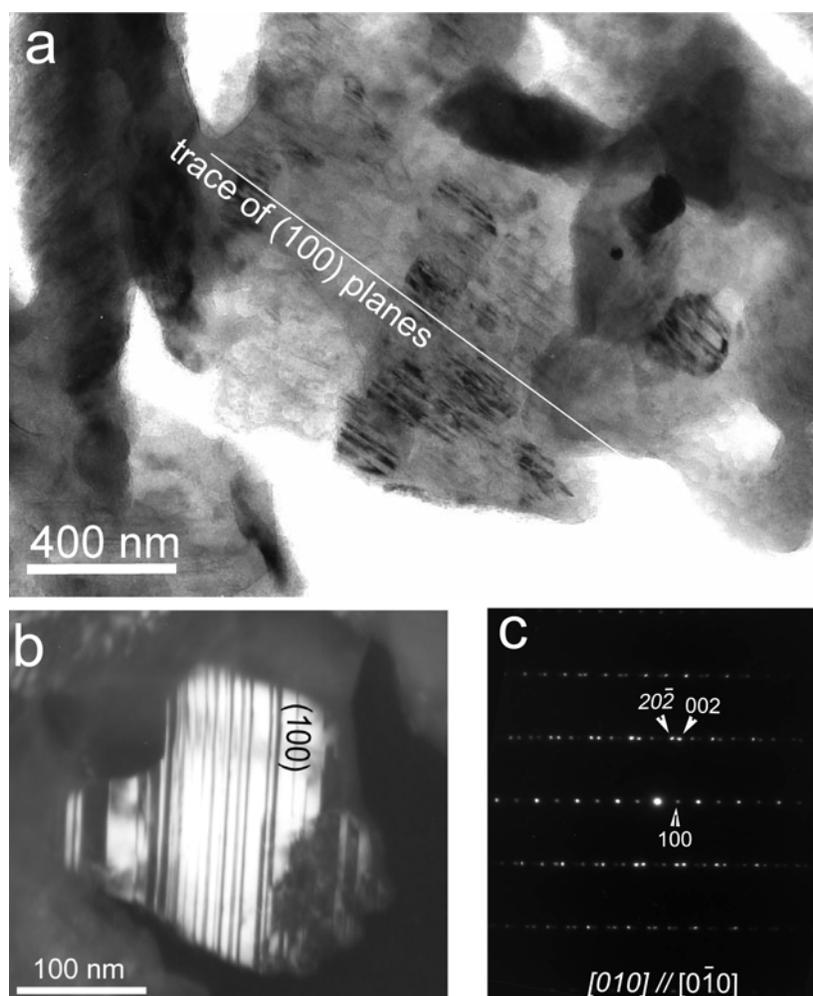
Fig. 3. Crystalline core of sample C2027,2,69,1,1. a) General view. The pyroxene grains exhibit a lamellar microstructure associated with twinning along (100). b) Dark-field image of a pigeonite grain with (100) planes oriented edge-on. Twinned domains exhibit strong contrast variations. c) Associated precession diffraction pattern corresponding to the superimposition of [010] and [0$\bar{1}$0] zone-axes of the $P2_1/c$ space group related by a mirror along (100) plane.

clinoenstatite lamellae (CLEN, space group $P2_1/c$, fringe spacing along (100) ~ 9 Å) in orthoenstatite (OEN, space group $Pbca$, fringe spacing ~18 Å). The basic structural unit of both structures are corner-sharing SiO_4 tetrahedra forming chains along the c-axis (Papike and Cameron 1976). CLEN consists of two alternating chains whereas OEN is made of four alternating chains. Thus, when (100) planes are oriented edge-on, the OEN lamellae exhibit a fringe spacing which is twice that of the CLEN. Among the observed samples, a distinction can be made as a function of their CLEN/OEN ratio.

CLEN-Poor Samples: C2027,2,69,2,2 and C2027,3,32, 2,2/3

In those samples, the ratio of CLEN in OEN is about 20% (Fig. 8). The CLEN phase generally appears as isolated double (100) lamellae, more rarely as stacks of even numbers of lamellae (between 4 and 14). The lamellae usually transect the entire shards, but some of

them stop in the OEN and are terminated by partial dislocations. These dislocations are invisible in dark-field images taken with **g = 400** and visible with **g = 002**, indicating a Burgers vector parallel to [001]. Some rare subgrain boundaries are found with lamellae stopping on them (Fig. 9), indicating that the lamellae postdate the sub-grain boundaries.

CLEN-Rich Sample: C2027,3,32,3,5

In this sample, the ratio of CEN lamellae is much higher, about 50% (Fig. 10). As a consequence, strong streaks parallel to the a^* direction appear on the SAED patterns. Lattice fringe images reveal in this case that the CEN domains are constituted of even or odd numbers of lamellae (Fig. 11). Some twinning is also observed between adjacent clinoenstatite domains. Similar observations have been recently reported on the same particle by Schmitz and Brenker (2008).
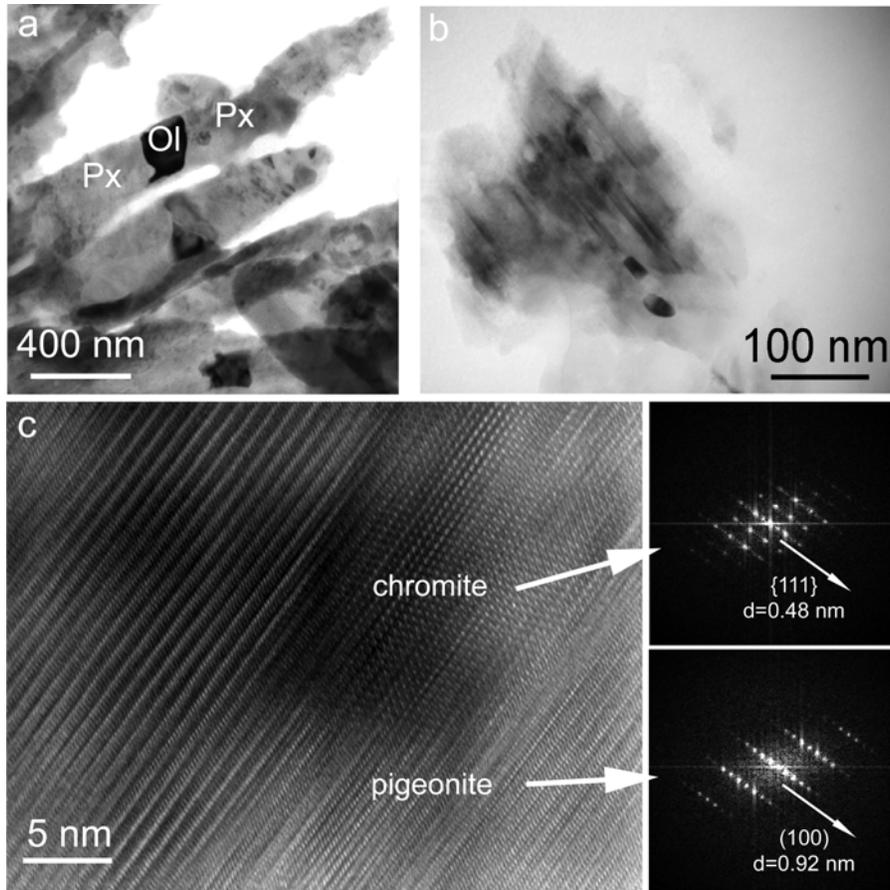
Fig. 4. Sample C2027,2,69,1,1. a) Olivine inclusions imbricate in pigeonite. b) Chromite inclusions in a twinned pigeonite host grain. c) High-resolution image of the chromite inclusion together with the Fourier transform diagrams of the chromite and pigeonite areas.
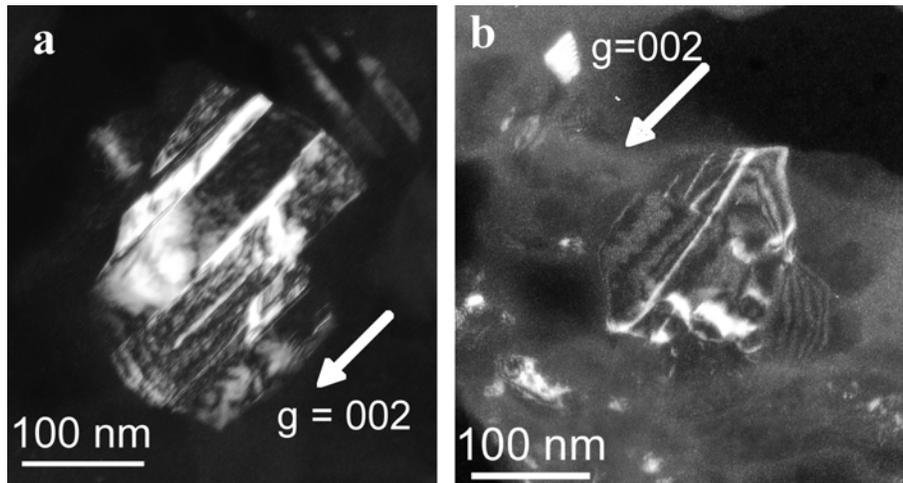

Fig. 5. Dark-field images of dislocations in sample C2027,2,69,1,1. a) In a pigeonite grain. b) In an olivine grain.

Dislocations

Free dislocations lying in the (100) planes of the orthoenstatite crystallites are observed in C2027,2,69,2,2, and C2027,3,32,2,2/3. They are elongated along the [100] direction and show small segments perpendicular to it (Fig. 12a). The long segments are visible with the diffraction vector g = **310** and invisible with g = **202**, which is compatible with b screw dislocations. Some other short segments visible with **202** are compatible with c Burgers vectors.
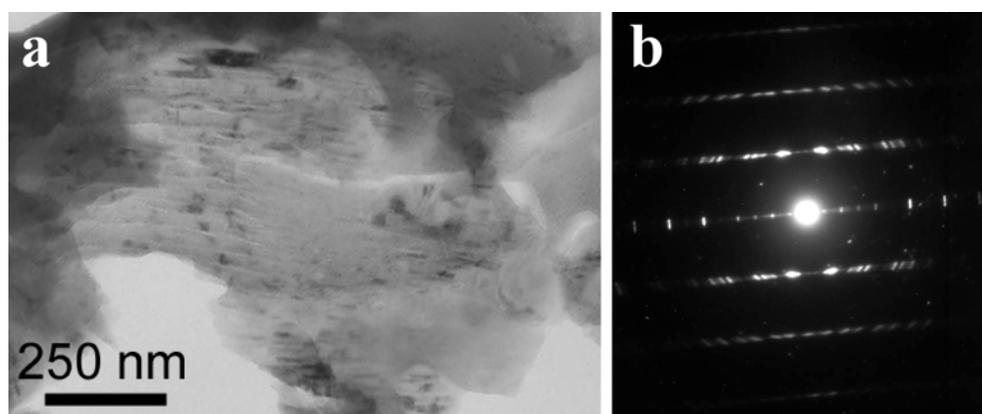
Fig. 6. Sample C2027,2,69,1,1. a) Bright-field image of a damaged pigeonite grain. b) Associated diffraction pattern along a [010] zone-axis. The mean orientation of the grain is the same as the surrounding twinned pigeonite grain.
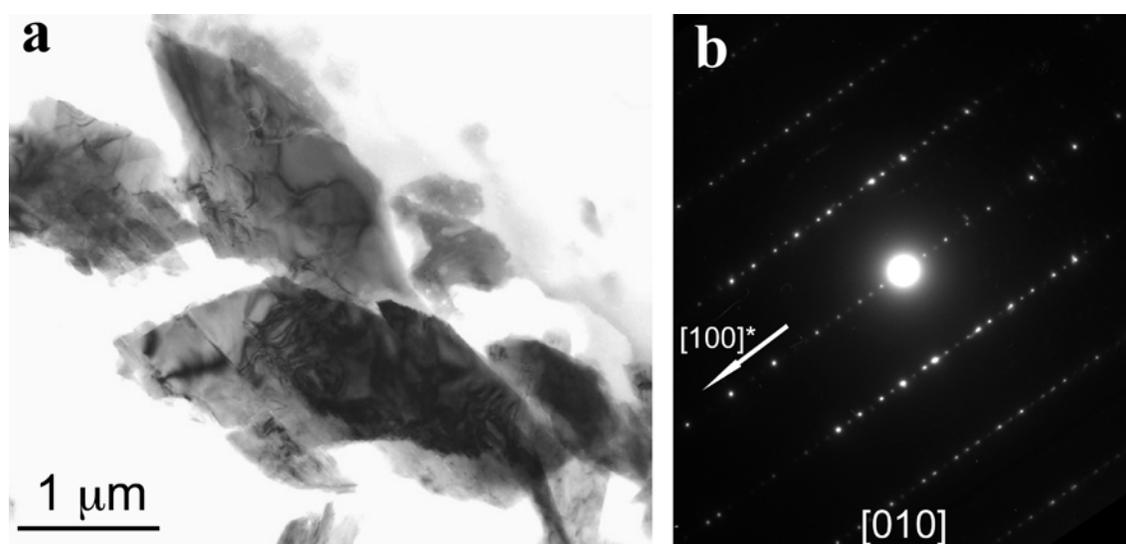

Fig. 7. Sample C2027,2,69,2,2. a) Bright-field image of an orthoenstatite grain. b) Corresponding SAED pattern along the [010] zone-axis (space group *Pbca*).

Exsolved Ca-Rich Grain in C2027,2,69,2,2

The Ca-rich grain found in C2027,2,69,2,2 exhibits a diopside-pigeonite exsolution microstructure on (001), with an average wavelength of 25 nm. A detailed description of this grain is given in Leroux et al. (2008b), and the main conclusions of this paper will be taken up in the discussion section. Dislocations are also present in this grain (Fig.12b). Dislocation lines cross the (001) lamellae but are also locally curved along (001) planes. This interaction indicates that the dislocation formation postdates the exsolution phenomena. As in the CPX grain (C2027,2,69,1,1), the diffraction-imaging experiments with various diffraction vectors suggest a *c* Burgers vector.

DISCUSSION

The four terminal particles studied in this work are coarse-grained pyroxenes that have survived the high-velocity capture in the collector. They appear relatively undamaged in comparison to the thermally modified grains frequently found in samples extracted from the wall tracks (Zolensky et al. 2006; Leroux et al. 2008a). They are single crystal particles several micrometers in diameter with a homogeneous microstructure. In the following discussion, we examine the possible origins of their main features: twinned pigeonite (C2027,2,69,1,1), CLEN lamellae in OEN (C2027,2,69,2,2, C2027,3,32,2,2/3 and C2027,3,32,3,5), and dislocations. The possible influence of the capture heating is also addressed.

Twinned Pigeonite

Pigeonite in sample C2027,2,69,1,1 contains a high density of (100) twins. Twinning in clinopyroxene can be obtained by two mechanisms: (1) quenching from the protopyroxene stability field and (2) plastic deformation
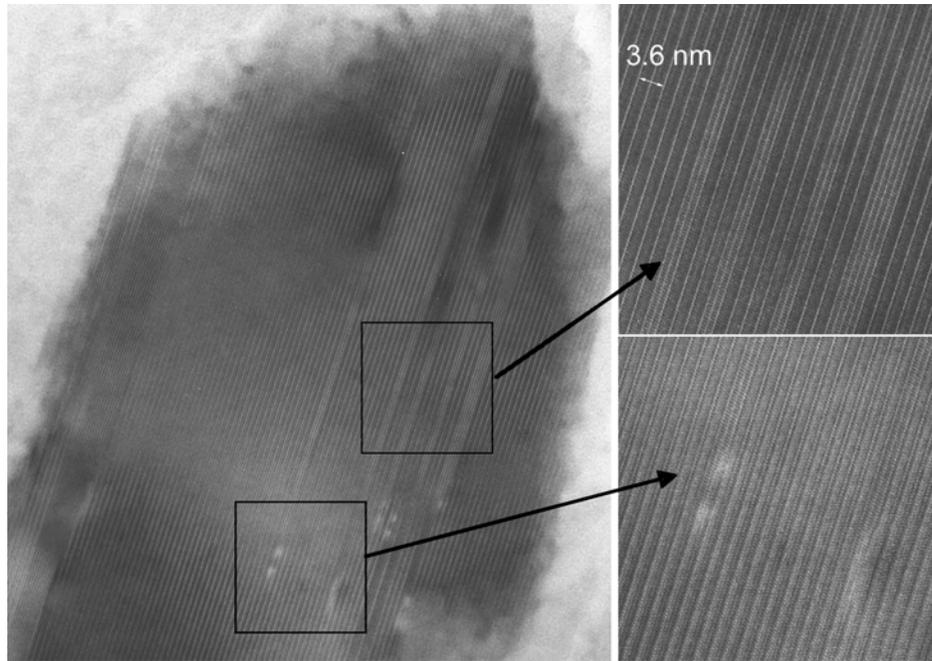
Fig. 8. Sample C2027,2,69,2,2. Lattice fringe image of an orthoenstatite grain. The 18 Å fringe spacing is associated with orthopyroxene whereas the 9 Å spacing corresponds to clinopyroxene. The CLEN phase generally appears as isolated double (100) lamellae, more rarely as stacks of even numbers of lamellae (between 4 and 14). When the clinopyroxene lamellae stop within the orthoenstatite matrix, some strain contrast associated to the stacking fault is observed.
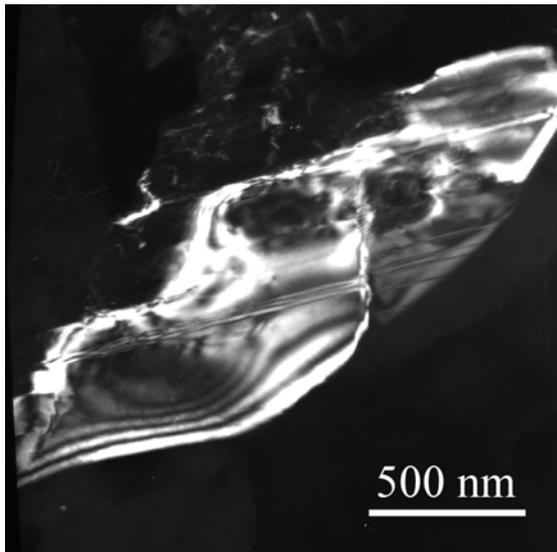

Fig. 9. Sample C2027,2,69,2,2. Dark-field image of (100) lamellae stopping on a grain boundary.

under high deviatoric stress (e.g., by shock deformation). For Ca-poor pyroxenes such as those observed in this sample, a high-temperature protopyroxene stability field extends for compositions ranging from pure enstatite to about $En_{80}Fs_{20}$ (Huebner 1980). Rapid cooling of protopyroxene (mechanism 1) leads to the formation of clinopyroxene with fine (100) polysynthetic twins, as observed experimentally

(Shimobayashi and Kitamura 1991) or in natural objects such as chondrules (Kitamura et al. 1983). In the case of plastic deformation (mechanism 2), the (100) twins occur as thin lamellae in the host, bordered by partial dislocations (Kirby and Christie 1977; Leroux et al. 1994). In our sample, the large fraction of twin domains (approximately 50%) and the absence of partial dislocations in the twin boundaries are not in agreement with a plastic deformation process. Thus, the twinned pigeonite microstructure of sample C2027,2,69,1,1 likely originates from cooling from the high temperature protopyroxene phase. Exsolution of chromite could have then occurred on further cooling.

CLEN Lamellae in Orthoenstatite

The dominant microstructure of the enstatite samples is the alternation of CLEN and OEN lamellae along the (100) planes. In C2027,2,69,2,2 and C2027,3,32,2,2/3 the CLEN/OEN ratio is about 20%, whereas it is about 50% in C2027,3,32,3,5. Furthermore, in the two first samples, CLEN domains are made of even numbers of lamellae, whereas in the latter, they are made of even or odd numbers, with occurrence of twinning. These differences must be related to different thermal histories. Indeed, following the review of Buseck et al. (1980), various possible mechanisms can be invoked to account for the observed mixed microstructures: (1) inversion from the high-temperature protoenstatite (PEN) stability field, (2) transformation from OEN by application of
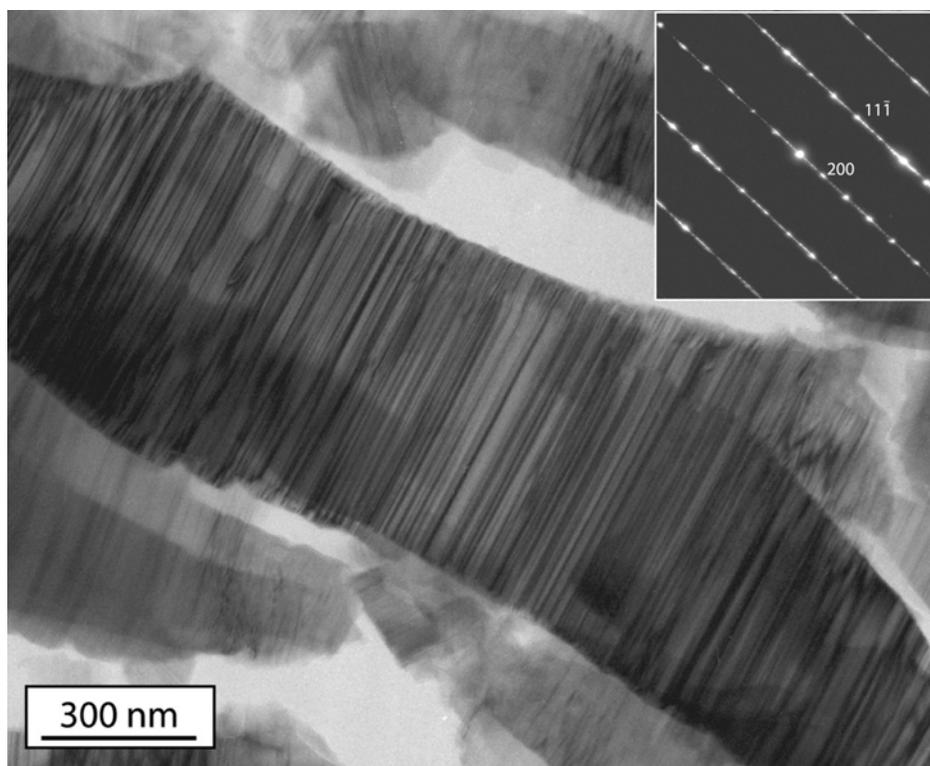
Fig. 10. Bright-field image of sample C2027,3,32,3,5 and the associated SAED pattern in the [011] zone axis orientation. Strong striking associated with stacking disorder is observed in the a^* direction.

homogeneous shear or shock, (3) static transformation from OEN. For the distinction between these various mechanisms, the widths and twinning of the CLEN lamellae are used. Direct inversion from the high-temperature PEN (mechanism 1) should lead to the formation of multiple 9 Å wide CLEN domains, with abundant twins and stacking disorder. CLEN domains that are produced from OEN (mechanisms 2 and 3) should be visible as multiples of 18 Å lattice repeats, since a single OEN lamella gives rise to a pair of CLEN lamellae. For mechanism 2, abundant twinning should be present only if the transformation is due to strong shock. If the transformation is shear-induced, no twinning is expected since the shear should result in most of the CLEN having a common orientation. For mechanism 3, the CLEN domains could exhibit the two twins orientation in approximately equal proportions. Following this classification, mechanism 1—cooling from the high temperature PEN—should be at the origin of the microstructure of sample C2027,3,32,3,5, whereas mechanisms 2 or 3—shear-induced or static transformation from OEN—could be responsible for the microstructure of samples C2027,2,69,2,2 and C2027,3,32,2,2/3. We consider here that the absence of twinning in the studied area of these two samples may be not representative of the entire samples, and thus that the distinction between either a shear-induced or a static transformation from OEN is not straightforward. There are abundant evidences that external stress favors the formation of clinopyroxene from orthopyroxene. The transformation is then martensitic in nature, with slip occurring on (100) planes. The transformation can also result from the passage through the crystal of partial dislocations with Burgers vector parallel to [001] (Coe and Kirby 1975; McLaren and Etheridge 1976). In our samples, the CEN lamellae often stop inside the OEN matrix, which suggests the formation via dislocation glide. Finally, in shocked OEN the CEN lamellae are abundant (e.g., Ashworth and Barber 1975; Ashworth 1985; Langenhorst et al. 1995; Leroux 2001), with pervasive twinning along (100). This is not the case for samples C2027,2,69,2,2 and C2027,3,32,2,2/3, for which this scenario can be excluded. In conclusion, the mixed CEN/OEN microstructures of the three enstatite samples are probably related to two types of mechanisms: cooling from the high temperature PEN phase for C2027,3,2,3,5 and direct inversion from OEN—either static or shear-induced—for samples C2027,2,69,2,2 and C2027,3,32,2,2/3.

Exsolved Diopside (C2027,2,69,2,2)

In C2027,2,69,2,2, a diopside grain has been found with an exsolution microstructure made of the alternating Ca-rich and Ca-poor lamellae parallel to (001) planes. In a previous paper (Leroux et al. 2008b), we have attributed the occurrence of this exsolved Ca-rich grain among a Ca-poor OEN to an igneous process, i.e., crystallization from a FeO-poor melt, pyroxene-like in composition, followed by a subsolidus
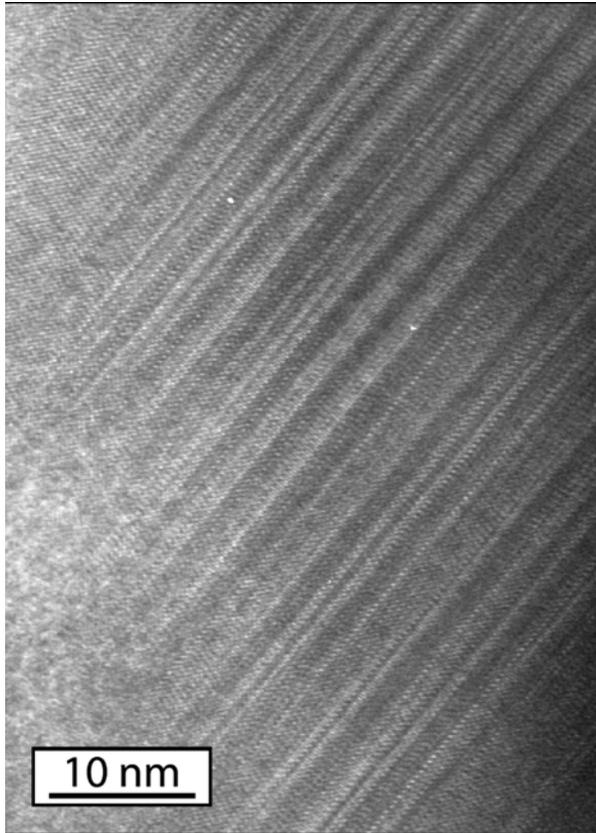
Fig. 11. Lattice fringe image of sample C2027,3,32,3,5.

exsolution process. Using the wavelength of the lamellae (25 nm) and a time-temperature transformation (TTT) diagram constructed with isothermal growths (Weinbruch and Müller 1995), the cooling rate has been estimated to 10–100 °C/h, within the temperature interval 1350–1200 °C. This cooling rate is very close to that of chondrule-like materials (Weinbruch and Müller 1995).

Dislocations: Evidence for Shock Deformation?

Dislocations have been found in all the samples. Free dislocations in olivine and pyroxene are generally clear indicators of shock deformation. The Stardust OEN grains (C2027,2,69,2,2, C2027,3,32,2,2/3) contain free dislocations in (100) with Burgers vectors [001] and [010] in edge orientation. These configurations correspond to the most active slip systems as observed in experimentally or naturally deformed orthopyroxene (Kohlstedt and Vander Sande 1973; McLaren and Etheridge 1976; Van Duysen et al. 1985; Nazé et al. 1987). In olivine grains found in C2027,2,69,1,1 dislocations have a Burgers vector [001] with screw orientation. This configuration is strongly dominant in shock-deformed olivine (e.g., Leroux [2001], and reference therein). The density of dislocations in olivine is increasing with the peak pressure but the olivine grains in C2027,2,69,1,1 are

small and the poor statistical occurrence preclude any speculation on the shock intensity. In clinopyroxene, i.e., pigeonite from C2027,2,69,1,1, the dislocations are screw [001] in (100). This configuration is once again the easiest activated glide system of clinopyroxene under shock deformation conditions (e.g., Leroux et al. 1994; Langenhorst et al. 1995). Partial [001] dislocations do not seem to be present in the twin walls of pigeonite as it might be the case for a shock deformation origin. In summary the dislocation microstructure observed in these samples is likely due to a shock event of small intensity. The occurrence of dislocations in glide configuration has already been reported in an olivine grain of Stardust samples (Tomeoka et al. 2008), and is also attributed to a shock origin. In Stardust samples, the peak pressure associated with the capture deceleration period into aerogel (Trigo-Rodríguez et al. 2008) could have reached a mean maximum value of 300 MPa, which is about one order of magnitude smaller than the Hugoniot elastic limit of pyroxene and olivine. Application of this peak pressure during the very brief period of capture (1 µs) is not expected to induce some dislocations motion, suggesting that the dislocations microstructure was established prior to the capture. Nevertheless, stress concentration within the particle is possible, leading to higher local stress values. Furthermore, heating of the collected grains is attested by the occurrence of the melt rim around the samples. The rapid heating and cooling of the particles during the collect could have induced a thermal shock, associated with high thermal gradient acting on an anisotropic elastic media such as pyroxene. This may also have contributed to the dislocations motion during capture.

Heating Effect

The interpretation of the microstructure of Stardust material is rendered complex because of the possible high-temperature regime that may have occurred during the capture deceleration. The capture of particles in aerogel has been demonstrated to induce local melting due to the hypervelocity impact at 6.1 km s^{-1} in the silica aerogel collectors (Zolensky et al. 2006; Leroux et al. 2008a; Roskosz et al. 2008). The melted material has been quenched as a glass mixed with silica coming from melted silica aerogel. This easily recognized microstructure is not observed in our samples, except at the periphery of the particles. Thus, if the studied pyroxene grains have been prevented from melting, they may have undergone a short excursion at high temperature. If the temperature exceeded 1000 °C the enstatite grains could have entered into the high temperature PEN stability field. The transformation from CEN to PEN (and reverse) is very fast (Smyth 1974), martinsitic in nature, whereas the transformation from ortho- to proto-pyroxene, which requires a coordinated motion of alternating pairs of octahedral layers, is very sluggish (Smyth
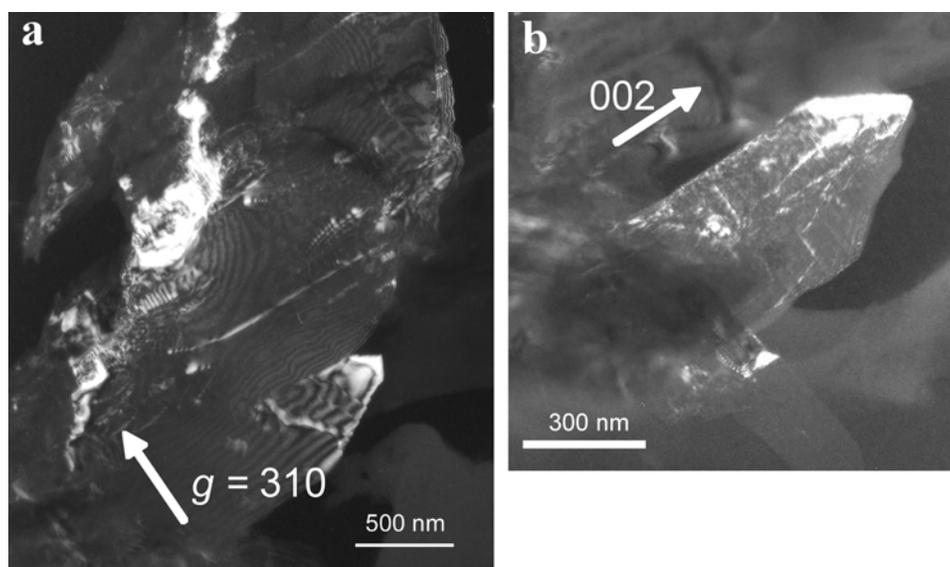
Fig. 12. Dark-field images of dislocations in sample C2027,2,69,2,2. a) In an orthoenstatite grain. b) In the exsolved diopside grain.

1974). If the grain was originally CEN rich, as C2027,3,32,3,5, some modifications of the microstructure may have then occurred. It is also the case of sample C2027,2,69,1,1 (Fe-rich clinopyroxene), but in that case the required temperature to reach the PEN domain is around 1400 °C. Nevertheless, in this sample, the presence of chromite exsolution on the twin boundaries, which requires time at high temperature, favors the twins formation before the capture process. For the OEN- rich samples such as C2027,2,69,2,2 and C2027,3,32,2,2/3, even if the PEN domain was reached, some time would have been needed to induce the sluggish transformation of OEN, much more than that of the high temperature period deduced from the observation of melted material in Stardust samples (Roskosz et al. 2008). Concerning the exsolved diopside grain in C2027,2,69,2,2, the cooling rate of 10–100 °C (Leroux et al. 2008b) appears much lower than the one deduced from the thermal regime associated to the capture (Roskosz et al. 2008), showing that the formation of an exsolution microstructure in pyroxene during the capture is unrealistic. In conclusion, we are likely to argue that the entire microstructures reported here are pristine, i.e., associated to natural pre-capture events.

Nevertheless, some possible small modifications of the pristine microstructures are possible. Indeed, as previously noticed concerning dislocations motion, even if 1000 °C was not reached, high thermal gradients are likely in the Stardust samples due to rapid heating and cooling. Thermal shear stresses must then have been produced. In these conditions the formation of clino-lamellae in orthoenstatite, as that observed in samples C2027,2,69,2,2, C2027,3,32,2,2/3, and C2027,3,32,3,5 is likely since this deformation process is starting at relatively low shear stress >70 MPa (Coe and Kirby 1975).

CONCLUSIONS

We have reported the detailed microstructure of four terminal particles coming from two neighboring tracks (69 and 32, cell 27) of Stardust collector. The two terminal particles from track 69 strongly differ. Particle 1 consists of twinned pigeonite: $En_{75}Wo_4 Fs_{21}$ with minor olivine Fo_{76-83}. The twinned microstructure is not usual in pigeonite and is probably related to its specific FeO content and a corresponding protoenstatite—pigeonite transition at relatively high temperature (typically around 1400 °C). Particle 2 is an almost pure enstatite single crystal (average $En_{95}Wo_2Fs_3$). The CEN lamellae distribution is compatible with an OEN to CEN transition, likely assisted by a shear stress because of the presence of dislocations terminating CEN lamellae. The microstructure does not show evidence for a signature of a PEN-OEN transition, suggesting a moderate or low cooling after the crystal formation (supposing it formed at high temperature). Observation in this particle of an exsolved diopside grain is fully consistent with an igneous formation process, with a cooling rate similar to that of chondrule-like materials. Igneous textures or potential chondrule-bearing minerals have been identified in other Wild 2 particles (Zolensky et al. 2006; Joswiak et al. 2007; Nakamura et al. 2008), showing that chondrule-like objects are found not only in meteorites but also in bodies assembled at large distances from the inner region of the solar system. This important finding, together with the discovery of calcium-aluminium-rich inclusions (CAIs) (Simon et al. 2008), supports the model of radial transport in the protoplanetary disk into the region of comet formation (Brownlee et al. 2006; Zolensky et al. 2006).

In track 32, both studied terminal particles (grain 2 and 3) are OEN with very close compositions (respectively En_{97-98}

$Wo_{0-1}Fs_{1-2}$ and $En_{94-95}Wo_{2-3}Fs_{2-4}$). However they strongly differ by their CEN/OEN ratio. Grain 3 probably acquired its high density of CEN lamellae during cooling from the PEN high-temperature phase field. It is not excluded that the grain experienced a high temperature regime during capture within the protoenstatite stability field. In contrast, grain 2 is rather compatible with a transition from OEN to CEN assisted by glide of partial dislocation in (100).

The pyroxene terminal grains in track 32 and 69 clearly demonstrate that the corresponding Wild 2 dusts were made by several coarse-grained silicates having different and probably unrelated origins. Differences are evidenced both by grain compositions and defect microstructures. These observations are important to constrain the comet grain model. The Wild 2 dust is likely a mixture between micro-sized silicates and very fine-grained material. The terminal particles likely correspond to the more resistant phases, i.e., the coarse-grained silicates. Some material is also present all along the track cavities but is found unfortunately largely melted. In this case the composition is frequently close to CI (Leroux et al. 2008a; Stephan et al. 2008) and the deduced original grain size is more than one order smaller than the terminal particles. All these observations lead to conclude that dust particles which impacted the aerogel capture medium were weakly bound aggregates constituted by one or several large silicate grains together with a very fine grained matrix.

The defect microstructure in pyroxene is comparable to those already reported in chondritic meteorites. Twinned pigeonite was observed in chondrules (Kitamura et al. 1983), as well as the exsolved diopside with comparable lamellae wavelength (Weinbruch and Müller 1995). Clinopyroxene lamellae microstructure in orthopyroxene is a very frequent defect microstructure in meteorites. Following Ishii et al. (2008), we conclude that terminal particles closely resemble to chondritic meteorite minerals.

The presence of free dislocations as well as the partial dislocations in OEN are clear indicators for shock deformation. The relatively low density of dislocations suggests nevertheless a moderate shock. The deformation features may probably have formed prior to the high-velocity capture into aerogel because the peak pressure due to the capture is probably lower than 0.3 GPa, i.e., well below the Hugoniot elastic limit of silicates (Trigo-Rodríguez et al. 2008). Nevertheless the exceptional physical conditions of the capture include a possible intense thermal pulse. A thermal shock as possible cause for the observed microstructures cannot be ruled out. We expect that the in coming comparison at the microscopic scale of pre- and post-capture microstructures of experimentally shocked materials will help clarify this point.

Editorial Handling—Dr. Anthony Jones

REFERENCES

Ashworth J. R. and Barber D. J. 1975. Electron petrography of shock effects in a gas-rich enstatite achondrite. *Contributions to Mineralogy and Petrology* 49:149–162.

Ashworth J. R. 1985. Transmission electron microscopy of L-group chondrites, 1. Natural shock effects. *Earth and Planetary Science letters* 73:17–32.

Brownlee D., Tsou P., Aléon J., Alexander C. M. O'D., Araki T., Bajt S., Baratta G. A., Bastien R., Bland P., Bleuet P., Borg J., Bradley J. P., Brearley A., Brenker F., Brennan S., Bridges J. C., Browning N. D., Brucato J. R., Bullock E., Burchell M. J., Busemann H., Butterworth A., Chaussidon M., Cheuvront A., Chi M., Cintala M. J., Clark B. C., Clemett S. J., Cody G., Colangeli L., Cooper G., Cordier P., Daghlian C., Dai Z., D'Hendecourt L., Djouadi Z., Dominguez G., Duxbury T., Dworkin J. P., Ebel D. S., Economou T. E., Fakra S., Fairey S. A. J., Fallon S., Ferrini G., Ferroir T., Fleckenstein H., Floss C., Flynn G., Franchi I. A., Fries M., Gainsforth Z., Gallien J.-P., Genge M., Gilles M. K., Gillet Ph., Gilmour J., Glavin D. P., Gounelle M., Grady M. M., Graham G. A., Grant P. G., Green S. F., Grossemy F., Grossman L., Grossman J. N., Guan Y., Hagiya K., Harvey R., Heck P., Herzog G. F., Hoppe P., Hörz F., Huth J., Hutcheon I. D., Ignatyev K., Ishii H., Ito M., Jacob D., Jacobsen C., Jacobsen S., Jones S., Joswiak D., Jurewicz A., Kearsley A. T., Keller L. P., Khodja H., Kilcoyne A. L. D., Kissel J., Krot A., Langenhorst F., Lanzirotti A., Le L., Leshin L. A., Leitner J., Lemelle L., Leroux H., Liu M.-C., Luening K., Lyon I., MacPherson G., Marcus M. A., Marhas K., Marty B., Matrajt G., McKeegan K., Meibom A., Mennella V., Messenger K., Messenger S., Mikouchi T., Mostefaoui S., Nakamura T., Nakano T., Newville M., Nittler L. R., Ohnishi I., Ohsumi K., Okudaira K., Papanastassiou D. A., Palma R., Palumbo M. E., Pepin R. O., Perkins D., Perronnet M., Pianetta P., Rao W., Rietmeijer F. J. M., Robert F., Rost D., Rotundi A., Ryan R., Sandford S. A., Schwandt C. S., See T. H., Schlutter D., Sheffield-Parker J., Simionovici A., Simon S., Sitnitsky I., Snead C. J., Spencer M. K., Stadermann F. J., Steele A., Stephan T., Stroud R., Susini J., Sutton S. R., Suzuki Y., Taheri M., Taylor S., Teslich N., Tomeoka K., Tomioka N., Toppani A., Trigo-Rodríguez J. M., Troadec D., Tsuchiyama A., Tuzzolino A. J., Tyliszczak T., Uesugi K., Velbel M., Vellenga J., Vicenzi E., Vincze L., Warren J., Weber I., Weisberg M., Westphal A. J., Wirick S., Wooden D., Wopenka B., Wozniakiewicz P., Wright I., Yabuta H., Yano H., Young E. D., Zare R. N., Zega T., Ziegler K., Zimmermann L., Zinner E., and Zolensky M. 2006. Comet 81P/Wild 2 under a microscope. *Science* 314:1711–1716.

Burchell M. J., Fairey S. A. J., Wozniakiewicz P., Brownlee D. E., Hörz F., Kearsley A. T., See T. H., Tsou P., Westphal A., Green S. F., Trigo-Rodríguez J. M., and Dominguez G. 2008. Characteristics of cometary dust tracks in Stardust aerogel and

laboratory calibrations. *Meteoritics & Planetary Science* 43:23–40.

Buseck P. R., Nord G. L., and Veblen D. R. 1980. Subsolidus phenomena in pyroxenes. In *Pyroxenes*, edited by Prewitt C. T. Reviews in Mineralogy, vol. 7. Washington, D.C.: Mineralogical Society of America. pp. 117–211.

Coe R. S. and Kirby S. H. 1975. The orthoenstatite to clinoenstatite transformation by shearing and reversion by annealing: Mechanism and potential applications. *Contributions to Mineralogy and Petrology* 52:29–55.

Davidson P. M. and Lindsley D. H. 1985. Thermodynamic analysis of quadrilateral pyroxenes. Part II: Model calibration from experiments and applications to geothermometry. *Contributions to Mineralogy and Petrology* 91:390–404.

Hörz F., Bastien R., Borg J., Bradley J. P., Bridges J. C., Brownlee D. E., Burchell M. J., Chi M., Cintala M. J., Dai Z. R., Djouadi Z., Dominguez G., Economou T. E., Fairey S. A. J., Floss C., Franchi I. A., Graham G. A., Green S. F., Heck P., Hoppe P., Huth J., Ishii H., Kearsley A. T., Kissel J., Leitner J., Leroux H., Marhas K., Messenger K., Schwandt C. S., See T. H., Snead C., Stadermann F. J. I., Stephan T., Stroud R., Teslich N., Trigo-Rodríguez J. M., Tuzzolino A. J., Troadec D., Tsou P., Warren J., Westphal A., Wozniakiewicz P., Wright I., and Zinner E. 2006. Impact features on Stardust: Implications for comet 81P/Wild 2 dust. *Science* 314:1716–1719.

Huebner J. S. 1980. Pyroxene phase at low pressure. In *Pyroxenes*, edited by Prewitt C. T. Reviews in Mineralogy, vol. 7. Washington, D.C.: Mineralogical Society of America. pp. 213–288.

Ishii H. A., Bradley J. P., Dai Z. R., Chi M., Kearsley A. T., Burchell M. J., Browning N. D., and Molster F. 2008. Comparison of comet 81P/Wild 2 dust with interplanetary dust from comets. *Science* 319:447–450.

Joswiak D. J., Matrajt G., Brownlee D. E., Westphal A. J., and Snead C. J. 2007. A roedderite-bearing terminal particle from Stardust track 56: Comparison with rare peralkaline chondrules in ordinary chondrites (abstract #2142). 38th Lunar and Planetary Science Conference. CD-ROM.

Kirby S. H. and Christie J. M. 1977. Mechanical twinning in diopside Ca(Mg,Fe)Si$_2$O$_6$: Structural mechanisms and associated crystal defects. *Physics and Chemistry of Minerals* 1:137–163.

Kitamura M., Yasuda M., Watanabe S., and Morimoto N. 1983. *Earth and Planetary Science Letters* 63:189–201.

Kohlstedt D. L. and Vander Sande J. B. 1973. Transmission electron microscopy investigation of the defect microstructure of four natural orthopyroxenes. *Contributions to Mineralogy and Petrology* 42:169–180.

Langenhorst F., Joreau P., and Doukhan J. C. 1995. Thermal and shock metamorphism of the Tenham chondrite: A TEM examination. *Geochimica et Cosmochimica Acta* 59:1835–1945.

Leroux H., Doukhan J. C., and Langenhorst F. 1994. Microstructural defects in experimentally shocked diopside: A TEM characterization. *Physics and Chemistry of Minerals* 20:521–530.

Leroux H. 2001. Microstructural shock signatures of major minerals in meteorites. *European Journal of Mineralogy* 13:253–272.

Leroux H., Devouard B., Cordier P., and Guyot F. 2004. Pyroxene microstructure in the Northwest Africa 856 Martian meteorite. *Meteoritics & Planetary Science* 39:711–722.

Leroux H., Rietmeijer F. J. M., Velbel M. A., Brearley A. J., Jacob D., Langenhorst F, Bridges J. C., Zega T. J., Stroud R. M., Cordier P., Harvey R. P., Lee M., Gounelle M., and Zolensky M. 2008a. A TEM study of thermally modified comet 81P/Wild 2 dust particles by interactions with the aerogel matrix during the Stardust capture process. *Meteoritics & Planetary Science* 43:97–120.

Leroux H., Jacob D., Stodolna J., Nakamura-Messenger K., and Zolensky M. 2008b. Igneous Ca-rich pyroxene in 81P/Wild 2 comet. *American Mineralogist* 93:1933–1936.

Lindsley D. H. 1983. Pyroxene Thermometry. *American Mineralogist* 68:477–493.

Lindsley D. H. and Andersen D. J. 1983. A two-pyroxene thermometer. *Journal of Geophysical Research* 88:A887–A906.

McCallister R. H. and Nord G. L. 1981. Subcalcic diopsides from kimberlites: Chemistry, exsolution microstructures, and thermal history. *Contribution to Mineralogy and Petrology* 78:118–125.

McLaren A. C. and Etheridge M. A. 1976. A transmission electron microscope study of naturally deformed orthopyroxene. *Contributions to Mineralogy and Petrology* 57:163–177.

Nakamura T., Noguchi T., Tsuchiyama A., Ushikubo T., Kita N. T., Valley J. W., Zolensky M. E., Kakazu Y., Sakamoto K., Mashio E., Uesugi K., and Nakano T. 2008. Chondrule-like objects recovered from short-period comet 81P/Wild 2. *Science* 321:1664–1667.

Nazé L., Doukhan N., Doukhan J. C., and Latrous K. 1987. A TEM study of lattice defects in naturally and experimentally deformed orthopyroxenes. *Bulletin de Minéralogie* 110:497–512.

Papike J. J. and Cameron M. 1976. Crystal Chemistry of Silicate Minerals of Geophysical Interest. *Review of Geophysics* 14:37–80.

Papike J. J. 1996. Pyroxene as a recorder of cumulate formational processes in asteroids, Moon, Mars, Earth: Reading the record with the ion microprobe. *American Mineralogist* 81:525–544.

Papike J. J., Karnet J. M., and Shearer C. K. 2005. Comparative planetary mineralogy: Valence state partitioning of Cr, Fe, Ti, and V among crystallographic sites in olivine, pyroxene, and spinel from planetary basalts. *American Mineralogist* 90:277–290.

Roskosz M., Leroux H., and Watson H. C. 2008. Thermal history, partial preservation and sampling bias recorded by Stardust cometary grains during their capture. *Earth and Planetary Science Letters* 273:195–202.

Ross M. and Huebner J. S. 1979. Temperature-composition relationships between naturally occurring augite, pigeonite, and orthopyroxene at one bar pressure. *American Mineralogist* 64:1133–1155.

Schmitz S. and Brenker F. 2008. Microstructural indications for protoenstatite precursor of cometary MgSiO$_3$ pyroxene: A further high temperature component of comet Wild 2. *The Astrophysical Journal* 681:L105–L108.

Shimobayashi N. and Kitamura M. 1991. Phase transition in Ca-poor clinopyroxenes. *Physics and Chemistry of Minerals* 18:153–160.

Simon S. B., Joswiak D. J., Ishii H. A., Bradley J. P., Chi M., Grossman L., Aléon J., Brownlee E., Fallon S., Hutcheon I. D., Matrajt G., and McKeegan K. D. 2008. A refractory inclusion returned by Stardust from comet 81P/Wild 2. *Meteoritics & Planetary Science* 43:1861–1877.

Smyth J. R. 1974. Experimental study of the polymorphism of enstatite. *American Mineralogist* 59:345–352.

Stephan T., Rost D., Vicenzi E. P., Bullock E. S., MacPherson G. J., Westphal A. J., Snead C. J., Flynn G. J., Sandford S. A., and Zolensky M. 2008. TOF-SIMS analysis of cometary matter in Stardust aerogel tracks. *Meteoritics & Planetary Science* 43:233–246.

Tomeoka K., Tomioka N., and Ohnishi I. 2008. Silicate minerals and Si-O glass in comet Wild 2 samples: Transmission electron microscopy. *Meteoritics & Planetary Science* 43:273–284.

Trigo-Rodríguez J. P., Dominguez G., Burchell M. J., Hörz F., and Llorca J. 2008. Bulbous tracks arising from hypervelocity capture in aerogel. *Meteoritics & Planetary Science* 43:75–86.

Van Duysen J. C., Doukhan N., and Doukhan J. C. 1985. Transmission electron microscope study of dislocations in

orthopyroxene (Mg,Fe)$_2$Si$_2$O$_6$. *Physics and Chemistry of Minerals* 12:39–44.

Vincent R. and Midgley P. A. 1994. Double conical beam-rocking system for measurement of integrated electron diffraction intensities. *Ultramicroscopy* 53:271–282.

Weinbruch S. and Müller W. F. 1995. Constraints on the cooling rates of chondrules from the microstructure of clinopyroxene and plagioclase. *Geochimica et Cosmochimica Acta* 59:3221–3230.

Zema M., Tarantino S., Domeneghetti M. C., and Tazzoli V. 2003. Ca in orthopyroxene: Structural variations and kinetics of the disordering process. *European Journal of Mineralogy* 15:373–380.

Zolensky M. E., Zega T. J., Yano H., Wirick S., Westphal A. J., Weisberg M. K., Weber I., Warren J. L., Velbel M. A., Tsuchiyama A., Tsou P., Toppani A., Tomioka N., Tomeoka K., Teslich N., Taheri M., Susini J., Stroud R., Stephan T., Stadermann F. J., Snead C. J., Simon S. B., Simionovici A., See T. H., Robert F., Rietmeijer F. J. M., Rao W., Perronnet M. C., Papanastassiou D. A., Okudaira K., Ohsumi K., Ohnishi I., Nakamura-Messenger K., Nakamura T., Mostefaoui S., Mikouchi T., Meibom A., Matrajt G., Marcus M. A., Leroux H., Lemelle L., Le L., Lanzirotti A., Langenhorst F., Krot A. N., Keller L. P., Kearsley A. T., Joswiak D., Jacob D., Ishii H., Harvey R., Hagiya K., Grossman L., Grossman J. N., Graham G. A., Gounelle M., Gillet Ph., Genge M. J., Flynn G., Ferroir T., Fallon S., Ebel D. S., Dai Z. R., Cordier P., Clark B., Chi M., Butterworth A. L., Brownlee D. E., Bridges J. C., Brennan S., Brearley A., Bradley J. P., Bleuet P., Bland P. A., and Bastien R. 2006. Mineralogy and petrology of comet 81P/Wild 2 nucleus samples. *Science* 314:1735–1739.

Zolensky M., Nakamura-Messenger K., Rietmeijer F., Leroux H., Mikouchi T., Ohsumi K., Simon S., Grossman L., Stephan T., Weisberg M., Velbel M., Zega T., Stroud R., Tomeoka K., Ohnishi I., Tomioka N., Nakamura T., Matrajt G., Joswiak D. Brownlee D., Langenhorst F., Krot A., Kearsley A., Ishii H., Graham G., Dai Z. R., Chi M., Bradley J., Hagiya K., Gounelle M., and Bridges J. 2008a. Comparing Wild 2 particles to chondrites and IDPs. *Meteoritics & Planetary Science* 43:261–272.

Zolensky M., Nakamura-Messenger K., Fletcher L., and See T. 2008b. Curation, spacecraft recovery and preliminary examination for the Stardust mission: A perspective from the curatorial facility. *Meteoritics & Planetary Science* 43:5–21.